https://doi.org/10.1016/j.compositesa.2022.107221

Wrinkled, Cracked and Bridged Carbon Networks for Highly Sensitive and Stretchable Strain Sensors

*Dan Liu[1,2//], Heng Zhang[2//], Haomin Chen[2], Jeng-Hun Lee[2], Fengmei Guo[2], Xi Shen[*3], Qingbin Zheng[*1], and Jang-Kyo Kim[*2]*

[1]School of Science and Engineering, The Chinese University of Hong Kong, Shenzhen, Guangdong 518172, China.

[2]Department of Mechanical and Aerospace Engineering, The Hong Kong University of Science and Technology, Clear Water Bay, Kowloon, Hong Kong.

[3]Department of Aeronautical and Aviation Engineering, The Hong Kong Polytechnic University, Hung Hom, Kowloon, Hong Kong.

* Correspondence and requests for materials should be addressed to Qingbin Zheng (zhengqingbin@cuhk.edu.cn) or Xi Shen (xi.shen@polyu.edu.hk) or Jang-Kyo Kim (mejkkim@ust.hk)

KEYWORDS: Strain sensor, Wrinkle, Crack, Carbon network, Highly Stretchable and Sensitive.

ABSTRACT

With rapid advance of wearable electronics technologies, flexible strain sensors having both high sensitivity and high stretchability are highly desired. In this work, inspired by lotus roots whose fibers remain joined even after fracture, highly sensitive and stretchable strain sensors are designed using single-walled carbon nanotube (SWNT)/graphene oxide (GO) hybrid thin films with unique wrinkled, cracked and bridged morphologies. The distinctive wrinkled and cracked structure is created by tuning the pre-stretching releasing of the hybrid film on a silicone rubber substrate. Under tension, the myriad SWNTs bridged the wrinkled film by sliding within the hybrid film giving rise to high stretchability, while the nano/microscale cracks provide the strain sensor with a high sensitivity through tunneling. Thanks to the synergy arising from the wrinkles, cracks and bundles bridged the cracks, the hybrid sensor exhibits a wide sensing range of 100%, an ultrahigh gauge factor of 2000 with excellent stability for over 1000 cycles. These exceptional properties enable the sensor to monitor full range human motions from tiny eye blinks to large joint movements. A wearable gaming controller is prototyped using the developed sensor to demonstrate voice-empowered maneuver of car racing games.

1. Introduction

Wearable strain sensors with high flexibility and sensitivity are becoming increasingly important because of their diverse applications in human-machine interfaces[1], human motion detection[2], electronic skins[3], personalized health monitoring[4,5], and soft robotics[6]. Among many types of strain sensors based on piezoresistivity, piezoelectricity, triboelectricity, Raman shifting, fiber Bragg gratings, and capacitance, piezoresistive sensors have been widely used due to its simple read-out mechanism, superior sensitivity, and cost-effective fabrication[7,8]. Traditional

piezoresistive strain sensors made from metal foils or semiconducting crystals are usually rigid and fragile, making them difficult to be integrated with other flexible devices. In addition, since the piezoresistive behavior of a traditional strain sensor arises mainly from the piezoresistance of the material itself, the gauge factor (GF) - the ratio of relative change in electrical resistance R to the mechanical strain ε - provided by geometric effects is relatively small, ranging from 1.0 ~ 5.0[9].

Aiming to obtain stretchable and adequately sensitive strain sensors, various nanomaterials has been utilized and a variety of new structures have been developed simultaneously[10]. Metal nanoparticles[11], metal nanowires[12], silicon nanoribbons[13], conductive polymers[14], MXene[15,16], and carbon materials including fullerene[17], carbon nanotubes (CNTs)[18], graphene[19,20], carbon nanofiber[21], graphite[22], carbon black[23], carbon dots[24] and carbonized silk[25] have been explored along with elastomer substrates. Among them, CNT and graphene have attracted much attention because of their outstanding flexibility, conductivity and transparency[26-30]. For the CNT-based strain sensor, spring-like CNT films produced by pre-stretching and releasing the strain allowed an elongation of up to 150%[31]. Thin films of aligned single-walled carbon nanotubes (SWNTs) with fractured gaps, islands and bundles were capable of measuring strains of up to 280%[2]. A multi-walled CNT (MWNT) film sandwiched between natural rubber layers were stretched up to 620%[32]. CNT-based strain sensors offer extremely high elongations, but their GF values is usually poor[33-35]. For the graphene-based strain sensor, chemical vapor deposition (CVD) synthesized graphene film showed GFs about 14 with a maximum strain of ~7%[36-41], because its hexagonal structure is partially destroyed, altering the electronic band structure and the electrical resistance under low tensile strains. Furthermore, nanographene[42-44], graphene woven fabric[20], graphene foam[45], graphene aerogel[46],

graphene hydrogel[47] and graphene/polymer composites[48-53] were explored to increase the sensitivity and stretchability. Graphene-based strain sensors offer high GFs, but their stretchability is hard to be improved. Although the intrinsic properties of nanomaterials are important, the structure of nanomaterials has a huge impact on the performance of the strain sensor. Wrinkle structure, crack structure, serpentine structure and grid structure have been widely used to further improve the performance of strain sensor [53-59]. Among them, wrinkle structure can effectively enhance the stretchability due to pre-stored stress and crack structure can dramatically increase the sensitivity because of the rapidly changed number of conductive paths induced by cracks. Though wrinkle and crack structures have been applied in many kinds of above-mentioned nanomaterials, simultaneously improving the stretchability and sensitivity through wrinkle and crack structures is still very hard. Therefore, comprehensive consideration of material selection and structural design is important for preparing high-performance strain sensor.

Nature often offers inspirations for innovative and rational design of new materials and structures. Through millions of years of evolution, biomaterials such as lotus root have developed amazing properties largely resulting from the fiber-reinforced axially porous structure [60]. For example, when lotus roots are fractured, the fibers drawn out from the broken stems effectively bridging them (**Figure 1a**). As a Chinese old saying goes, “Literally lotus roots may break, but the fiber remains joined”, which is typically used to describe the fact that “Lovers part, but still long for one another”. Inspired by the structure of lotus roots, we fabricated highly sensitive and stretchable strain sensors by designing a new kind of wrinkled and cracked structure based on SWNT/GO hybrid film. Because the conductivity of SWNT is better than MWNT and the aspect ratio of SWNT is higher than that of MWNT under the condition of equal mass. Therefore, SWNT was used here instead of MWNT. As schematically illustrated in **Figure 1b**, a carbon network is

established through the formation of nano/microcracks and bridging the separate carbon islands. The hybrid strain sensors with wrinkled, cracked and bridged carbon network (WCBCN) present substantially improved sensitivity and stretchability. They sustained strains up to 100% with a remarkable maximum GF of 2,000 and durable stability for over 1,000 cycles. Equipped with both exceptionally high stretchability and sensitivity, these sensors demonstrated niche applications requiring accurate monitoring of various human motions on a large scale and as a wearable gaming controller.

2. Results and Discussion

Figure 1c schematically illustrates the key processes for fabricating SWNT/GO hybrid sensors with WCBCN structure. The synthesis process of GO is essentially similar to our previous reports.[17] As shown in **Figure S1**, most of GO sheets are single or few layers and the size of GO sheets is mainly larger than 10 μm. SWNT/GO hybrid films were first produced on filter membrane by vacuum filtration described previously.[17] Five types of films with different mass ratios of SWNTs to GO were fabricated to identify an optimal composition, namely 1:0, 5:1, 2:1, 1:1, and 0:1, while their thicknesses were kept the same by controlling the total volume in the dispersion. The Raman spectra of SWNT/GO hybrid films shown in **Figure S2** also confirm the existence of SWNTs and GO. Upon increasing the SWNT content, the G-band peak position upshifted and the D- to G-band intensity ratio, I_D/I_G, decreased, as expected. To create the unique wrinkled and cracked morphologies, the hybrid films combined with filter membrane was transferred onto a pre-strained polydimethylsiloxane (PDMS) substrate. To assist a successful transfer of hybrid films, a thin layer of uncured PDMS liquid was coated on the surface of PDMS substrate followed by a constant pressure and curing to make the hybrid film strongly adheres to the PDMS substrate and create intimate contact between SWNTs and GO. Then, the filter membrane was easily peeled off

from SWNT/GO hybrid films because the interaction between hybrid films and PDMS is much stronger than that between hybrid films and filter membrane. After the release of pre-strain (30%), the wrinkled and cracked structure was obtained. A larger stretching strain (100%) was further applied to widen the crack followed by releasing to obtain stable WCBCN hybrid film.

(a)

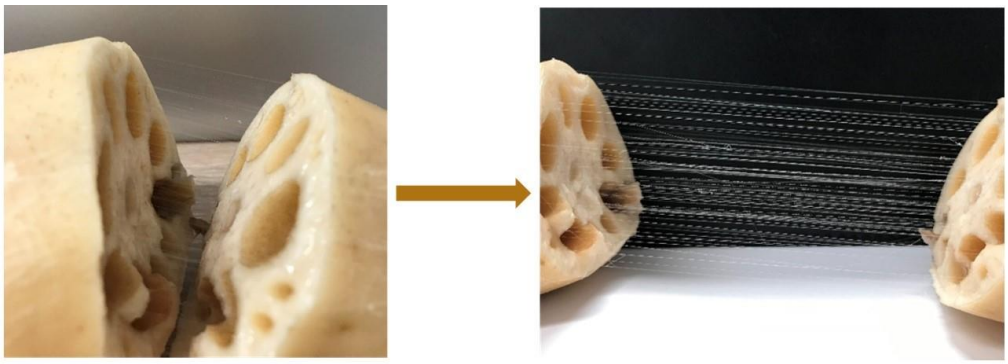

(b)

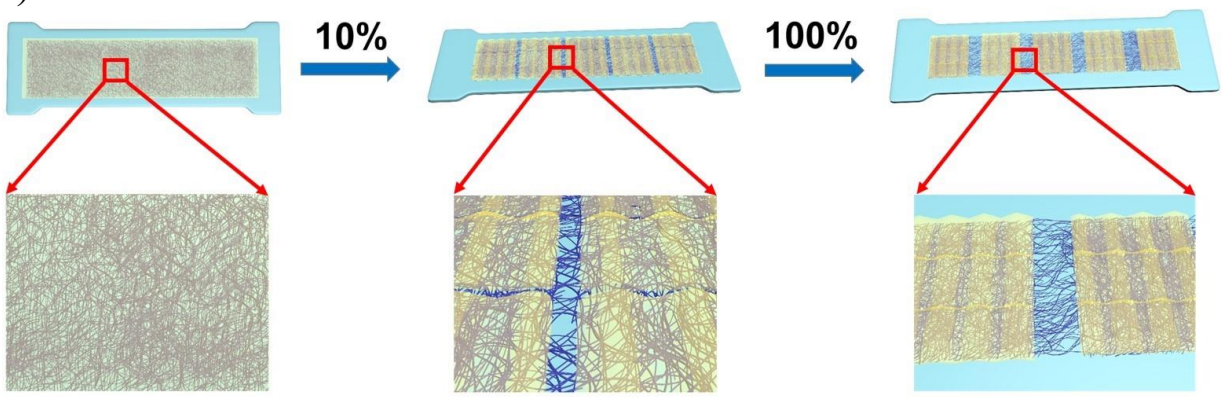

(c)

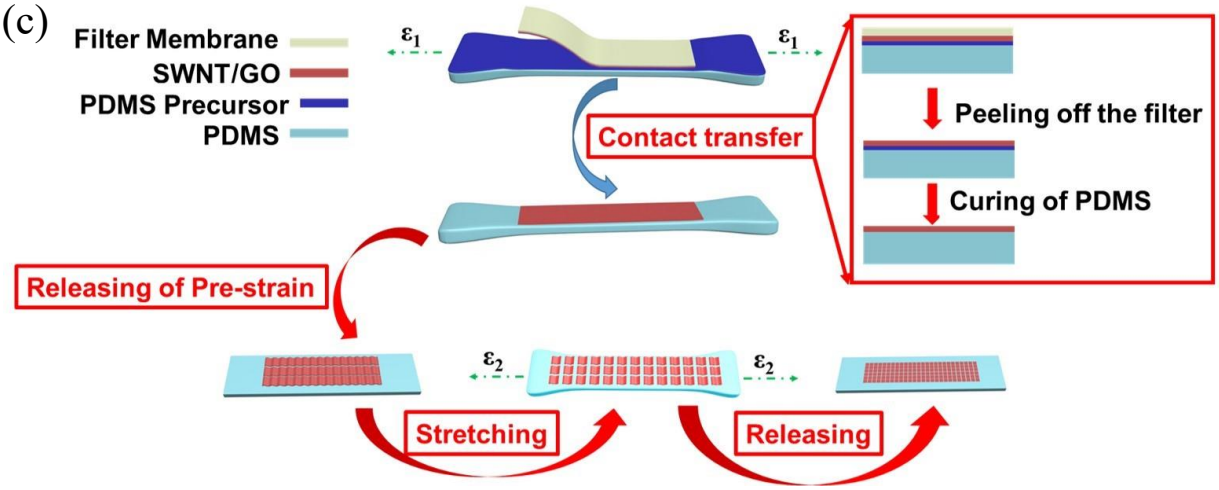

Figure 1. Schematic diagrams. (a) Fractured lotus root bridged by numerous fibers drawn out of broken surface; (b) Illustration of the concept of lotus root-inspired WCBCN structure; (c) Schematic flowchart of the fabrication procedure of the WCBCN strain sensor using SWNT/GO hybrid film on a PDMS substrate.

The techniques of releasing moderate strains of thin films along a pre-stretched direction to produce unidirectional wrinkles have been well developed. However, it is interesting to notice that releasing a much higher pre-strain (up to 100%) not only produced unidirectional wrinkles, but also periodic cracks. As shown in **Figure 2a-c** and **Figure S3**, the reduced graphene oxide (rGO) film transferred to a pre-stretched elastomer substrate initially displayed a flat morphology. Upon release of uniaxial pre-strain in the substrate, the rGO film developed wrinkles and cracks (**Figure 2d-f** and **Figure S4**). The periodic microcracks were formed mainly due to the Poisson's ratio effect[61], which generates transverse tensile stress in response to the uniaxial compression of the substrate upon release of pre-strain. The transverse tension cracks the graphene film. A post-stretching was further applied after the releasing of pre-strain to stabilize the formed wrinkled and cracked structure (**Figure 2g**). As shown in **Figure 2h** and **Figure S5**, the wrinkled film was separated into many small rectangular shaped wrinkled slices when the mass ratio between SWNT and GO is 2:1. Most of these small wrinkled slices were surrounded by cracks and part of them are overlapped with adjacent slices. When the mass ratio between SWNT and GO is 5:1, the morphology of SWNT/GO hybrid film is similar while the density of wrinkle and crack is different (**Figure S6** and **S7**). The thickness of SWNT/GO hybrid films ranges from 1.0-1.5 μm (**Figure 2i**) through controlling the mass of SWNT and GO during the vacuum filtration. Since chemical functionalization process was not applied for SWNT during fabrication processes, it can be deduced that there was no chemical bonding between GO and SWNT. **Figure S8** shows the high-

magnification SEM images of SWNT/GO hybrid film. It is seen that the SWNTs were distributed evenly in hybrid films, indicating that SWNT is well dispersed in SWNT/GO due to the amphiphilic nature of GO.[57,58]

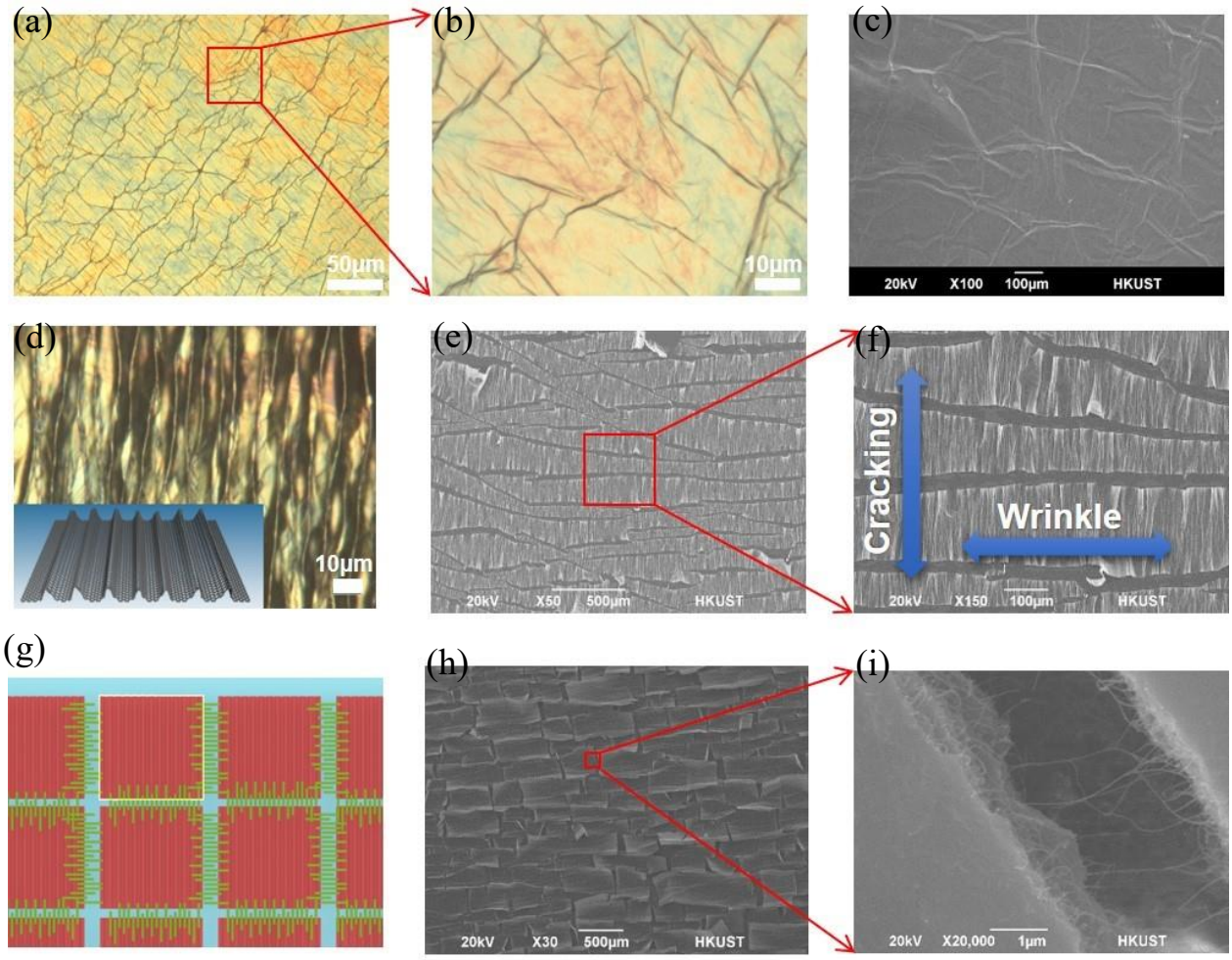

Figure 2. Top views of GO films before and after creating wrinkles and cracks. (a, b) Optical images and (c) SEM image of GO film on the PDMS substrate before the release of pre-strain; (d) Optical image of wrinkled GO film; (e, f) SEM images of a typical buckling pattern of GO film with transverse microcracks; (g) Schematic diagram of WCBCN SWNT/GO hybrid film (h, i) SEM images of WCBCN SWNT/GO hybrid film when mass ratios of SWNTs to GO is 2:1.

The microstructure and electromechanical performance of the wrinkled and cracked rGO films are firstly characterized (**Figure S9**). It can be seen that the wavelength of wrinkles (the length of one wrinkle along the pre-strain direction) inside rGO film, which is measured by SEM images, increases as the thickness of rGO film increases. The two-dimensional interconnected network structure with variable contact resistances between the cracked gaps upon straining demonstrated GFs of more than 150 depending on the level of pre-strains applied (**Figure 3a**). The high sensitivity is mainly due to tunneling through the opposite edges of the cracks. However, the resistance of a cracked thin film surged to almost infinity once the strain exceeded that of the tunneling regime of ~3%. Thus, the stretchability of these cracked rGO films was limited because of irreversible fractures even at a relatively low strain. This would restrict their value in detecting a full range of human motions, requiring a new strategy to hybridize GO with SWNTs to achieve a desired working range.

The sensing performance of SWNT/GO hybrid sensors with 30% pre-strain was investigated in comparison with that without pre-strain. As shown in **Figure 3b**, the 1D nature and high conductivity of SWNTs made the hybrid sensor even without pre-strain highly stretchable. Its GF decreased with increasing SWNT content, with a maximum GF of 20 at a SWNT/GO ratio of 2:1, while the sensitivity of neat SWNT film strain sensor was comparable to reported values 16. It is worth noting that the linearity was greatly improved with increasing GO, reaching a high coefficient of determination (R^2) of 0.99 at a SWNT/GO ratio of 2:1. More importantly, the GFs of hybrid sensors with 30% pre-strain were much higher than those without pre-strains, and a remarkable maximum GF of 2000 was achieved when the SWNT/GO ratio was 2:1 with a linearity of R^2=0.97, as shown in **Figure 3c**. Moreover, the WCBCN strain sensor (2:1) has a rapid response time, which is about 30 ms (Figure S10). The GF of WCBCN strain sensor is simultaneously

affected by the content of GO and SWNT. Because the GO is insulator, the increase of GO content results in higher GF and lower stretchability due to the decrease of the number of conductive paths. At the same time, the content of SWNT determines the connection efficiency of wrinkled pieces separated by cracks and the overall conductivity of SWNT/GO film. Therefore, the ratio of SWNT/GO is important for the performance of WCBCN strain sensor. As shown in Figure 3b, it can be deduced that the number of conductive paths and the connection efficiency of wrinkled islands separated by cracks reached the optimum state when the SWNT/GO ratio is 2:1, which shows a high GF of 2000.

The hybrid strain sensor showed excellent cyclic performance even at 100% strain (**Figure 3d, e**). The sensitivity of strain sensors depended on the maximum applied strain, according to **Figure S11**. The durability of the sensors was verified by stretching for more than 1000 cycles at 20% strain (**Figure 3g**). It is obvious that there were only negligible changes in relative resistance change after 1000 stretching cycles (**Figure S12**). The GFs and maximum sensing strains of various strain sensors fabricated with graphene and carbon nanotube films reported in the literature are compared in **Figure 3f**. It can be said that the CNT film-based strain sensors usually possess high stretchability but show low sensitivity, whereas the graphene film-based strain sensors have high sensitivity but present poor stretchability. These limitations occurring when each of CNT or

graphene film acted alone were overcome in this work where significant synergy was achieved by hybridizing SWNTs and GO to form a hybrid film with WCBCN.

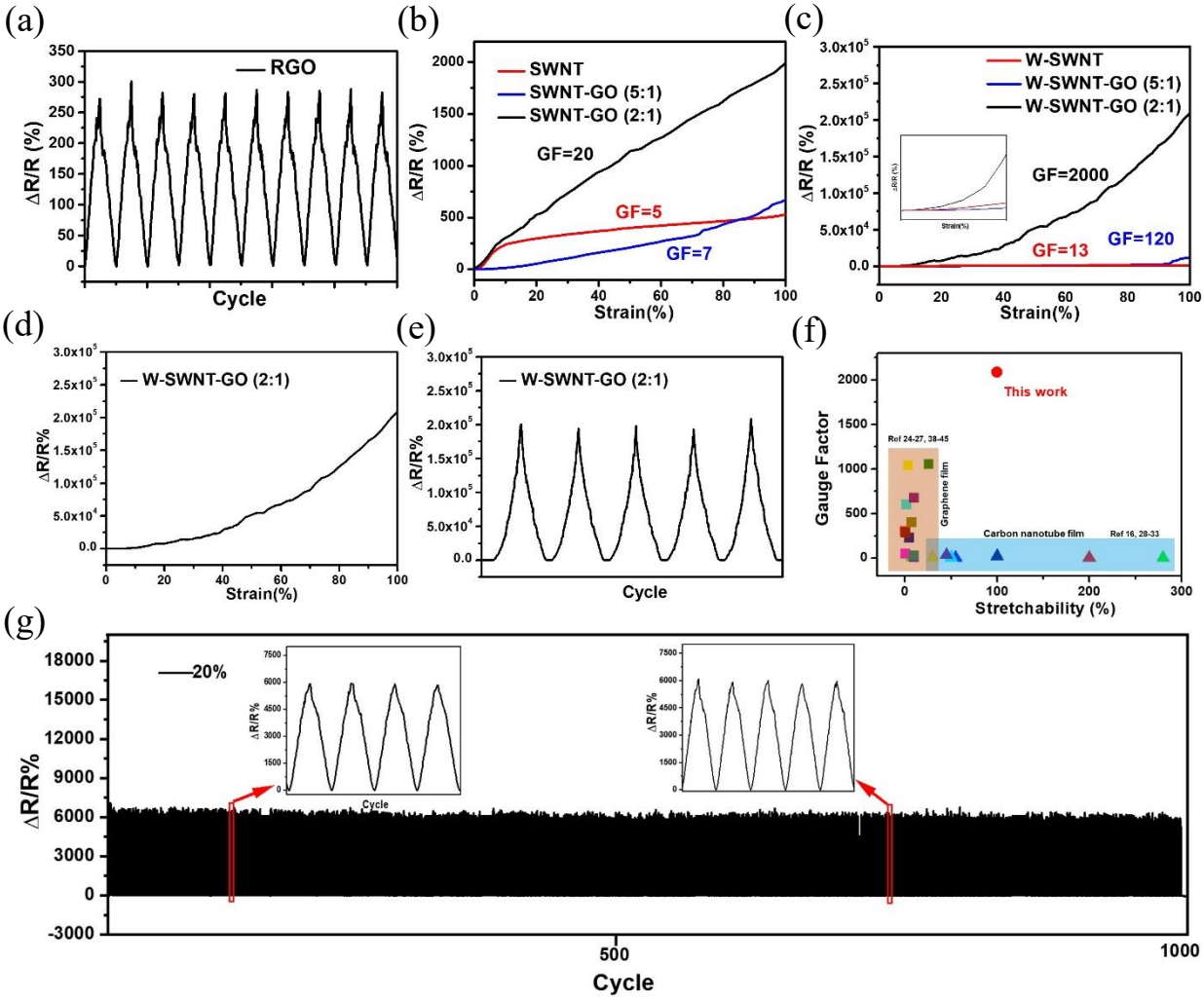

Figure 3. Characteristics of strain sensor. (a) Cycle performance of wrinkled rGO film strain sensor at a maximum strain of 2%; (b) Normalized resistance change at 100% strain of SWNT/GO hybrid film sensor without pre-strain; (c) Normalized resistance change at 100% strain of SWNT/GO hybrid film sensor with 30% pre-strain and the inset is enlarged image from 0-20% strain ; (d) Normalized resistance change, R/R_0, at 100% strain; (e) Cycle performance at 100% strain for 5 cycles; (f) Comparison of gauge factors and maximum sensing strains of various strain

sensors fabricated with graphene and carbon nanotube films reported in the literature; (g) Cycle performance at 20% strain for 1000 cycles.

To understand the underlying mechanism of the much-improved sensitivity and stretchability, the structural evolution of the SWNT/GO hybrid film with a SWNT/GO ratio of 5:1 was examined under different levels of strain (0-40%). The pre-stretched hybrid films contained quite uniformly-distributed cracks throughout the film, as shown in **Figure 4a**. At the initial state of stretching, the wrinkles flattened, the cracks started opening, resulting in lowered conduction paths (**Video S1**). Upon further stretching, the width of vertical crack gradually increased and paralleled crack decreased due to Poisson effect as the applied strain increases, which is similar with the process in **Figure 1b**. More importantly, the numerous SWNTs bundles not only embedded in the separate SWNT/GO islands through the van der Waals interactions, they also bridged the crack openings to connect the islands (**Figure 4b**). These SWNTs sustained a high tension between the split islands in alignment inside the SWNT/GO film, mimicking the lotus fibers that connect the fractured lotus root (**Figure 1a**). This accounts for the exceptional stretchability of the hybrid films compared with neat rGO films.

A simple model is proposed to predict the resistance change behaviors of the hybrid sensor based on WCBCN structure. According to foregoing discussions, the cracks running parallel and transverse to the loading direction underwent different reactions when a uniaxial tension was applied. The average width, W_1, of transverse cracks became larger than the initial width, W_0. In contrast, the average width, d_1, of paralleled cracks became smaller than the initial value, d_0, owing to the Poisson contraction. Assuming that all the wrinkle slices had the same resistance as the cracks connecting them where the tunneling effect dominated the resistance change, an equivalent circuit model was proposed, as shown in **Figure S13**. Because the flattening of wrinkles at the

initial stage of tension had a negligible effect on their conductive paths, the resistances of wrinkled slices remained constant during stretching. Therefore, the total resistance, R_{Total}, of the hybrid sensor containing *m* rows and *n* columns of slices is given by:

$$R_{total} = \frac{n}{2m}(4R_2 + R_1 + R_3) \quad (1)$$

where R_1 and R_3 represent the resistances of transverse and paralleled cracks, respectively, and R_2 refers to one quarter of the resistance of one wrinkled slice. Because R_1 and R_3 are dominated by tunneling resistance, they can be derived from the Simmons' equation:

$$R_1 = \frac{2wh^2}{3Ae^2\sqrt{2m_e\varphi}} exp\left(\frac{4\pi w\sqrt{2m_e\varphi}}{h}\right) \quad (2)$$

$$R_3 = \frac{2dh^2}{3A'e^2\sqrt{2m_e\varphi'}} exp\left(\frac{4\pi d\sqrt{2m_e\varphi'}}{h}\right) \quad (3)$$

where *w* and *d* are the tunneling distances of transverse and paralleled cracks, respectively. *A* and *A'* are the conduction area; φ and φ' are the potential heights from the Fermi level; m_e is the electron mass, *e* is the charge of electron and *h* is the Plank's constant. Thus, the total resistance change, $\Delta R/R_0$, can be written by (with the detail given in supporting information):

$$\frac{\Delta R}{R_0} = [Bg(\varepsilon) + Cf(\varepsilon)]\,\varepsilon^2 + [Dg(\varepsilon) - Ef(\varepsilon)]\varepsilon + g(\varepsilon) + f(\varepsilon) + F \quad (4)$$

where *B*, *C*, *D*, *E* and *F* are the constants, ε is the applied strain. The details of $g(\varepsilon)$ and $f(\varepsilon)$ can be found in supporting information.

The relationship between the relative resistance change and structural change associated with flattening of wrinkles, crack opening and closing can be reasonably explained by the tunnelling model, Equation (4), which fits well the experimental curve (**Figure 4c**). Because linear constants dominate in the fitted equation, the linearity of WCBCN strain sensor is excellent. From a quantitative perspective, the main reason for the high sensitivity of the hybrid strain sensor is that the cracks in the WCBCN structure remain in the range of tunnelling resistance at the initial state,

which is sensitive to the tunneling distance. For other ratios of SWNT/GO WCBCN strain sensor, the model also can be applied.

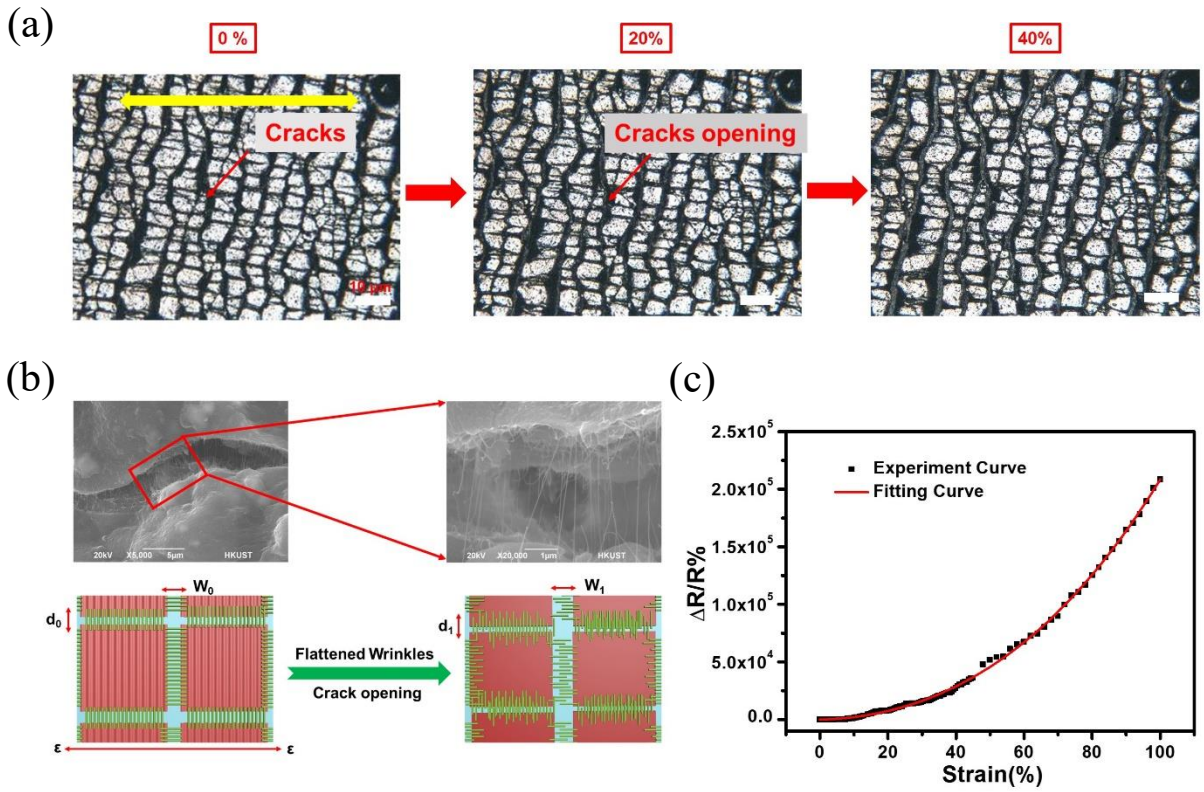

Figure 4. Mechanism of resistance change for WCBCN strain sensor under strain. (a) optical images of SWNT/GO hybrid film under different applied strains of 0%, 20% and 40%; (b) SEM images showing opened crack bridged by numerous SWNTs to give rise to high stretchability and schematic illustration of morphology change of WCBCN structure under tension; (c) Fitting of experimental curve of WCBCN strain sensor by tunneling model.

Taking advantage of the aforementioned outstanding sensitivity, excellent flexibility, broad working range, the applications of WCBCN strain sensors are demonstrated by detecting different kinds of human motions by attaching them on different body positions (**Figures 5a**). The WCBCN strain sensors are able to detect and distinguish the motions with different angles of arm and finger

(**Figures 5b-c**), even very small motions of eyes (**Figures 5d**). The strain induced by neck motion also can be detected, which is possible to used to correct neck posture, as shown in **Figure 5e**. The yawns usually indicate people's degree of fatigue, which may dangerously influence the driver's status. The WCBCN strain sensor can be used to warn the driver of drowsiness by examining the characteristic pattern of collected signals, as shown in **Figures 5f**. When the WCBCN strain sensor is attached on the knee (**Figure 5g**), it is convenient to measure steps and monitor the frequency of jumping.

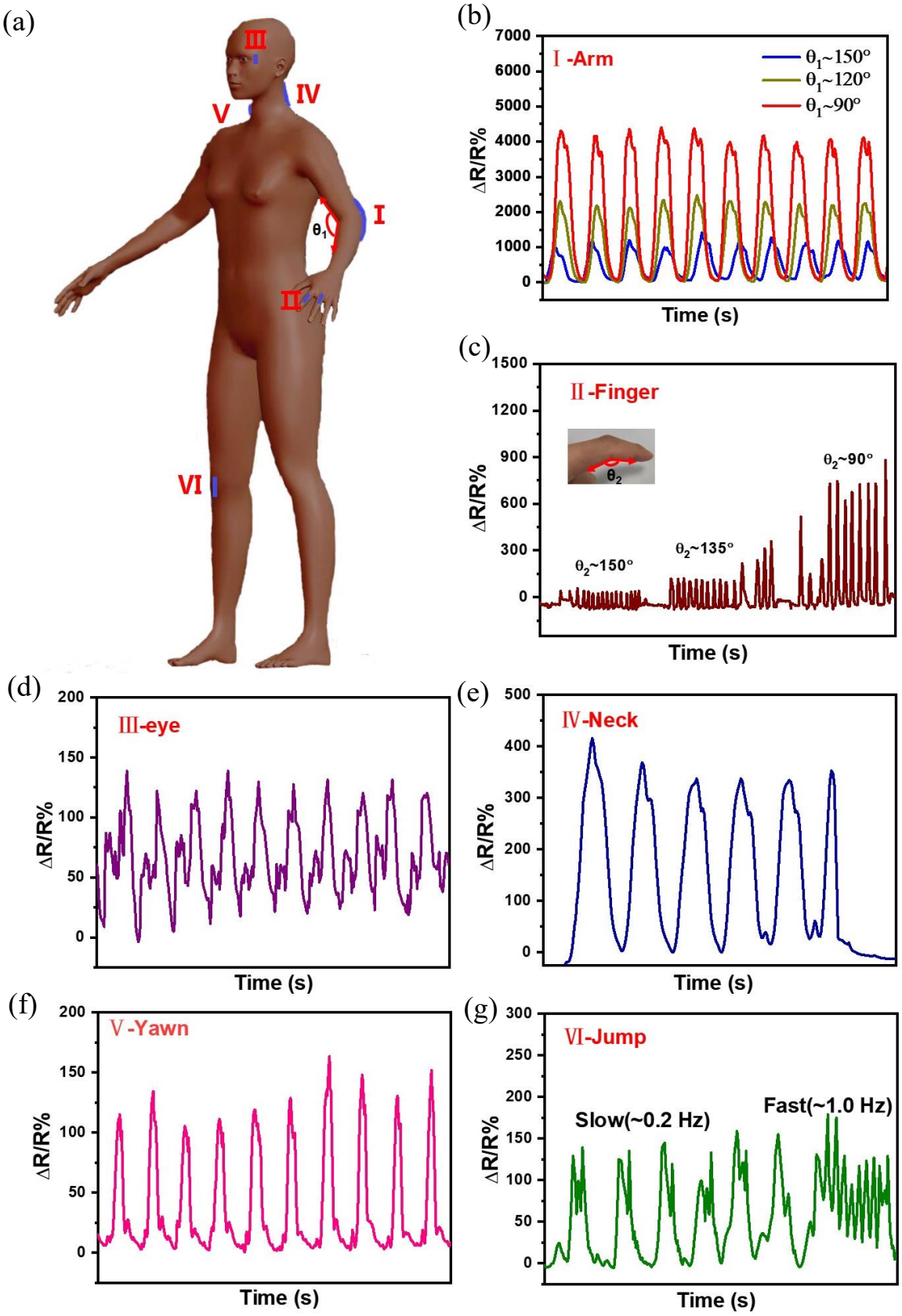
(a)
III
IV
V
I
θ1
II
VI
(b)
I -Arm
θ1~150°
θ1~120°
θ1~90°
ΔR/R%
Time (s)
(c)
II -Finger
θ2
θ2~90°
θ2~135°
θ2~150°
ΔR/R%
Time (s)
(d)
III-eye
ΔR/R%
Time (s)
(e)
IV-Neck
ΔR/R%
Time (s)
(f)
V -Yawn
ΔR/R%
Time (s)
(g)
VI-Jump
Slow(~0.2 Hz)
Fast(~1.0 Hz)
ΔR/R%
Time (s)

Figure 5. Applications of WCBCN strain sensors on human motions. (a) model of human body and positions strain sensors attached; (b-j) Monitoring of human motions, including arm (b), finger (c), eye(d), and neck (e) motions, yawn (f), and jump (g).

To further demonstrate the practical application of WCBCN strain sensor, the sensor outputs are implemented to autonomously control the cars in the virtual environment. Due to the high sensitivity of WCBCN strain sensor, the small strain induced by vibration of laryngeal prominence can be detected. As shown in the schematic diagram of the controller system in **Figure 6a**, two sensors are attached on the vocal cord and wrist respectively to record the subtle vibration strain and large joint bending deformation. Through connecting with a serial port control in Arduino, the physical signals of body motions are converted into the digital information in a real-time manner and then transferred into a terminal program in a computer. The gaming interface controller includes the speed adjustment and direction rotation. As the player produce a sound, the high voltage output from the movement of the vocal cord drove the model car to speed up, as shown in **Figure 6b**. The car stops moving when the voice is off. Similarly, the sensor on wrist joint commands the driving direction of the model car. In **Figure 6c**, the diverse bending states of the wrist, i.e., right, straight and left, generate different voltage signals, which are then mapped to the ration angle information. When the wrist is bent to the right, the sensor is in a compressed state and the conductive network is fully connected. The small resistance corresponds to 90° right rotation of the car model. As the wrist gradually recovers to the straight state and even bend left. The stretched sensing film leads to the large resistance increment and therefore the higher voltage which can command the car to go straight and turn left. The overall gaming control process could be found in **Video S2** (Supporting information).

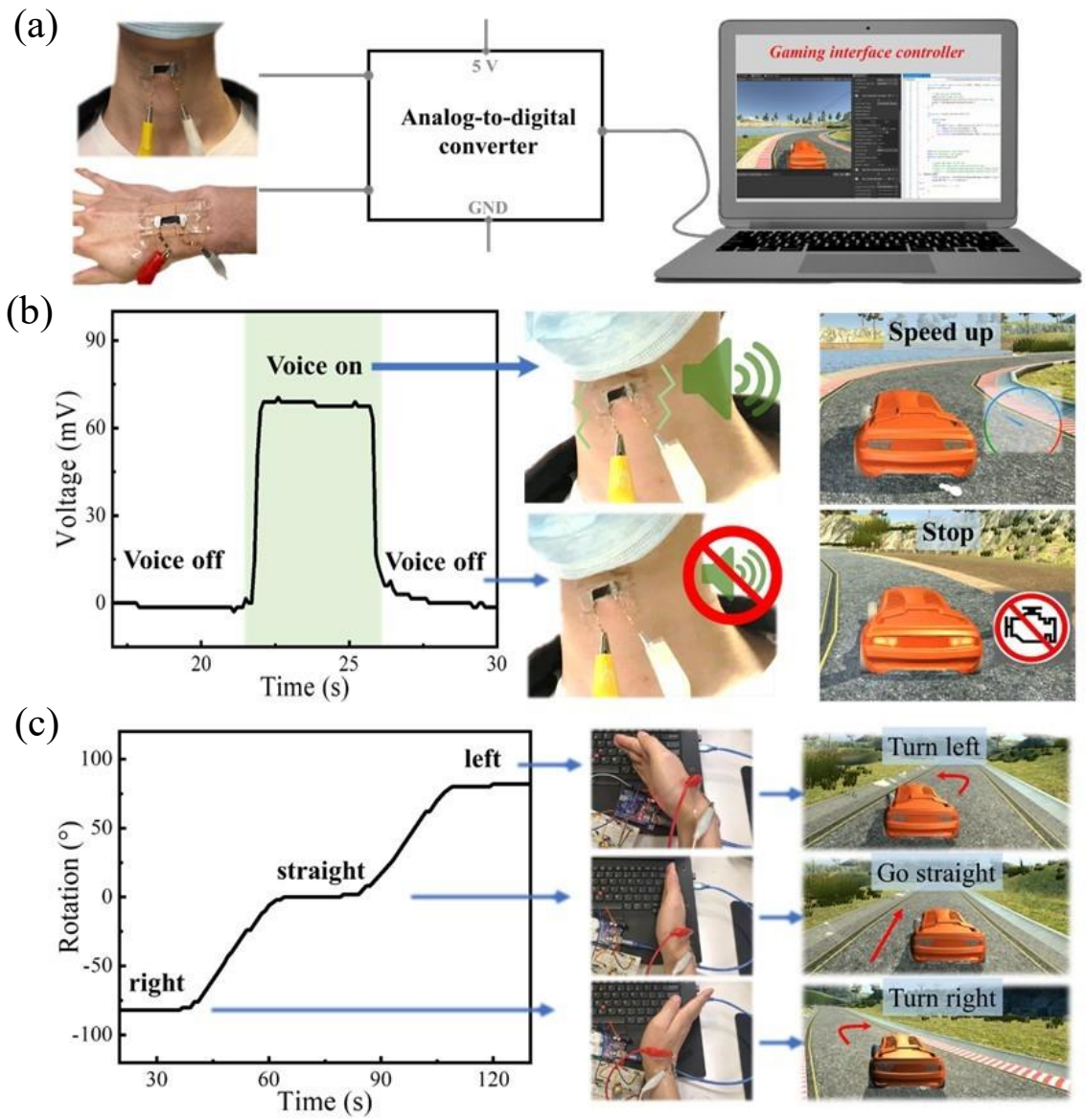

Figure 6. Wearable gaming controller application based on the WCBCN strain sensor. (a) Schematic illustration of the racing game controller system; (b) The collected signals from the voice enables the controlling of the car to speed up and stop; (c) The bending state of the wrist joint commands the car to perform corresponding actions including turning right, going straight and turning left.

3. Conclusion

In summary, inspired by fractured lotus root, we developed a high performance WCBCN strain sensor based on SWNT/GO hybrid film. By optimizing the ratio of SWNT/GO, the level of pre-strain and the film thickness, a balanced high performance with stretchability of 100%, GF of 2000 and $R^2 > 0.97$ is achieved. The high performance is mainly due to its unique structures including high density cracks and wrinkle slices with special bridged arrangement. It has been observed that the SWNT bundles inside cracks play an important role in connecting different wrinkle slices. A simple model is proposed to explain the experiment results by considering contact and tunneling resistance. The high performance of WCBCN strain sensor can be used to monitor human motions ranging from tiny to large motions, which can be implemented to play games in the virtual environment. This work represents a significant step towards the facile, low-cost, and scalable fabrication of ultra-sensitive and stretchable strain sensing devices using novel hybrid nanostructures with synergetic effects. The produced stretchable sensors may also be used in other emerging applications such as entertainment technology, robotics, and biomedicine.

Experimental Section

Synthesis of GO, rGO and SWNT/GO dispersion. To produce graphene at low costs, low temperature reduction will be performed to produce graphene with lateral dimensions from several to around a hundred micrometers based on our previous method.[17] GO was first synthesized via the modified Hummers method using natural graphite (supplied by Asbury Graphite Mills). A typical SEM images of the obtained of GO is shown in **Figure S1**. rGO was further synthesized by using N_2H_4 as a reducing agent. A typical process involves mixing 5 ml GO dispersion (2mg/ml), 160 µl N_2H_4 solution (30%) and 320 µl NH_3 followed by heating at 80℃ for 2 h to obtain well dispersed rGO solution. Sodium dodecyl sulfate (SDS) was used to disperse SWNT

(Chengdu organic chemicals co. LTD., Chinese Academy Science). A typical experiment involves mixing 20 mg SWNT, 200 mg SDS and 10 ml H2O. followed by tip sonication for 1h at 40% intensity. The SWNT/GO dispersion was prepared by mixing SWNT and GO Dispersion with different mass ratios.

Fabrication of WCBCN Strain Sensor. Spontaneous buckling with periodic cracks orthogonal to the buckled pattern was achieved through a facile pre-strain-stick-release assembly. First, a highly stretchable silicone rubber substrate will be uniaxially stretched to a large strain. rGO, SWNT or SWNT/GO hybrid film was then deposited on filter membrane *via* vacuum filtration and transfer printing on pre-stretched PDMS substrate. To obtain good adhesion between the films and substrates, the pre-stretched PDMS rubber substrates was coated with uncured liquid PDMS (the pre-mixed but unpolymerized PDMS and curing agent) followed by full curing (12h) once the film was transferred. After that, the filter membrane was peeled off from SWNT/GO hybrid films. Releasing the substrate's pre-strain formed delaminated buckling with periodic cracks due to the uniaxial compression. The formation of periodic cracks is mainly due to the Poisson's ratio effect, which generates transverse tensile stress in response to the uniaxial compression of the substrate. Finally, copper wires will be glued to the two ends of the film with silver paste to form a strain sensor. A thin layer of poly(methyl methacrylate) (PMMA) will be spin coated to encapsulate the percolation film with the purpose of increase the durability.

Fabrication of the gaming interface controller system. The data acquisition and analog-to-digital converter are through the Arduino chip (UNO REV3). The data are then transferred to the computer. The car racing game was built in the Unity. The connection of the data and controller of car speed and rotation direction was realized by game development programs that generated from source code.

Characterizations. An optical microscope (Olympus BX51M) and scanning electron microscopes (SEM, JEOL JSM-6390F) were used to characterize the surface and cross-section of rGO, SWNT and SWNT/GO films. The Raman spectra was obtained on a Micro-Raman spectrometer (Renishaw Micro-Raman/Photoluminescence System) using Ar ion laser (514.5 nm emission). The static and cyclic tensile tests of hybrid sensors were conducted on a universal testing machine (MTS Alliane RT-5) at cross-head speeds of 1mm/min. The resistances were monitored and collected simultaneously by a data logger (34970A Data Acquisition/Data Logger Switch Unit, Agilent).

Author Contributions

The manuscript was written through contributions of all authors. All authors have given approval to the final version of the manuscript. // Dan Liu and Heng Zhang contributed equally.

Conflicts of interest

There are no conflicts to declare.

Acknowledgements

This project was financially supported by the Research Grants Council of Hong Kong SAR (GRF projects: 16229216, 16209917 and 16205517), University Development Fund (UDF0100152), State Key Program of National Natural Science Foundation of China (Grant No. 51633007), the Program for Guangdong Introducing Innovative and Entrepreneurial Teams (Grant No. 2017ZT07C291), Shenzhen Science and Technology Program (Grant No. KQTD20170810141424366), Regional Joint Fund for Basic Research and Applied Basic Research of Guangdong Province (No. 2020SA001515110905), and Shenzhen Natural Science Foundation (GXWD20201231105722002-20200824163747001). Technical assistance from the Advanced

Engineering Materials facilities (AEMF) and the Materials Characterization and Preparation Facilities (MCPF) of HKUST is appreciated.

REFERENCES

[1] C. Z. Hang.; X. F. Zhao.; S. Y. Xi.; Y. H. Shang.; K. P. Yuan.; F. Yang.; Q. G. Wang.; J. C. Wang.; D. W. Zhang.; H. L. Lu. Highly stretchable and self-healing strain sensors for motion detection in wireless human-machine interface. *Nano Energy*, **2020**, *76*, 105064.

[2] N. Tang.; C. Zhou.; D. Y. Qu.; Y. Fang.; Y. B. Zheng.; W. W. Hu.; K. Jin.; W. W. Wu.; X. X. Duan.; H. Haick. A Highly Aligned Nanowire-Based Strain Sensor for Ultrasensitive Monitoring of Subtle Human Motion. *Small*, **2020**, *24*, 2001363.

[3] A. Chhetry.; S. Sharma.; S. C. Barman.; H. Yoon.; S. Ko.; C. Park.; S. Yoon.; H. Kim.; J. Y. Park. Black Phosphorus@Laser-Engraved Graphene Heterostructure-Based Temperature–Strain Hybridized Sensor for Electronic-Skin Applications. *Adv. Funct. Mater.* **2021**, *31*, 2007661.

[4] Q. B. Zheng.; X. Liu.; H. R. Xu.; M. S. Cheung.; Y. W. Choi.; H. C. Huang.; H. Y. Lei.; X. Shen.; Z. Y. Wang.; Y. Wu.; S. Y. Kim.; J. K. Kim. Sliced graphene foam films for dual-functional wearable strain sensors and switches. *Nanoscale Horiz.* **2018**, *3*, 35-44.

[5] N. Qaiser.; F. Al-Modaf.; S. M. Khan.; S. F. Shaikh.; N. El-Atab.; M. M. Hussain. A Robust Wearable Point-of-Care CNT-Based Strain Sensor for Wirelessly Monitoring Throat-Related Illnesses. *Adv. Funct. Mater.* **2021**, *31*, 2103375.

[6] S. Bauer.; S. Bauer-Gogonea.; I. Graz, M. Kaltenbrunner.; C. Keplinger.; R. Schwodiauer. Modeling and control of a soft robotic fish with integrated soft sensing. *Adv. Intell. Syst.* **2021**, 2000244.

[7] M. Amjadi.; K. U. Kyung.; I. Park, M. Sitti. Stretchable, skin-mountable, and wearable strain sensors and their potential applications: a review. *Adv. Funct. Mater.* **2016**, *26*, 1678-1698.

[8] Q. B. Zheng.; J. H. Lee.; X. Shen.; X. Chen.; J. K. Kim. Graphene-based wearable piezoresistive physical sensors. *Mater. Today* **2020**, *36*, 158-179.

[9] A. A. Barlian.; W. T. Park.; J. R. Mallon.; A. J. Rastegar.; B. L. Pruitt. Semiconductor piezoresistance for microsystems. *P Ieee* **2009**, *97*, 513-552.

[10] W. W. Wu.; H. Haick. Materials and Wearable Devices for Autonomous Monitoring of Physiological Markers. *Adv.Mater.***2018**, *30*, 1705024

[11] B. Ketelsen.; M. Yesilmen.; H. Schlicke.; H. Noei.; C.-H. Su.; Y.-C. Liao.; T. Vossmeyer. Fabrication of Strain Gauges via Contact Printing: A Simple Route to Healthcare Sensors Based on Cross-Linked Gold Nanoparticles. *ACS Appl. Mater. Interfaces* **2018**, *10*, 37374-37385.

[12] W. S. Lee.; D. Kim.; B. Park.; H. Joh.; H. K. Woo.; Y.-K. Hong.; T.-I. Kim.; D.-H. Ha.; S. J. Oh. Multiaxial and transparent strain sensors based on synergetically reinforced and orthogonally cracked hetero-nanocrystal solids. *Adv. Funct. Mater.* **2019**, *29*, 1806714.

[13] J. Kim.; M. Lee.; H. J. Shim.; R. Ghaffari.; H. R. Cho.; D. Son.; Y. H. Jung.; M. Soh.; C. Choi.; S. Jung.; K. Chu.; D. Jeon.; S. T. Lee.; J. H. Kim.; S. H. Choi.; T. Hyeon.; D. H. Kim. Stretchable silicon nanoribbon electronics for skin prosthesis. *Nat. Commun.* **2014**, *5*, 5747.

[14] H. J. Kim.; A. Thukral.; C. Yu. Highly sensitive and very stretchable strain sensor based on a rubbery semiconductor. *ACS Appl. Mater. Interfaces* **2018**, *10*, 5000-5006.

[15] Y. Yang.; L. Shi.; Z. Cao.; R. Wang.; J. Sun.; C. Ma.; M. G. Ma.; C. L. Si.; X. X. Ji.; P. B. Wan. Flexible MXene-Based Composites for Wearable Devices. *Adv. Funct. Mater.* **2021**, *31*, 2009524.

[16] L. H. Guo.; Z. K. Li.; W. W. Hu.; T. P. Liu.; Y. B. Zheng.; M. M. Yuan.; Y. J. Dai.; R. Z. Ning.; Y. J. Zhu.; K. Y. Tao.; M. Zhang.; T. Du.; L. Zhang.; C. Su.; H. Haick.; W. W. Wu. A flexible dual-structured MXene for ultra-sensitive and ultra-wide monitoring of anatomical and physiological movements. *J. Mater. Chem. A* **2021**, *9*, 26867-26874

[17] X. Shi.; S. Liu.; Y. Sun.; J. Liang.; Y. Chen. Lowering internal friction of 0D–1D–2D ternary nanocomposite-based strain sensor by fullerene to boost the sensing performance. *Adv. Funct. Mater.* **2018**, *28*, 1800850.

[18] J. Lee.; S. Pyo.; D.-S. Kwon.; E. Jo.; W. Kim.; J. Kim. Ultrasensitive strain sensor based on separation of overlapped carbon nanotubes. *Small* **2019**, *0*, 1805120.

[19] Q. B. Zheng.; W. H. Lp.; X. Y. Lin.; N. Yousefi.; K. K. Yeung.; Z. G. Li.; J. K. Kim. Transparent conductive films consisting of ultralarge graphene sheets produced by Langmuir–Blodgett assembly. *ACS Nano* **2011**, *5*, 6039-6051.

[20] X. Liu.; D. Liu.; J.-h. Lee.; Q. Zheng.; X. Du.; X. Zhang.; H. Xu.; Z. Wang.; Y. Wu.; X. Shen.; J. Cui.; Y.-W. Mai.; J.-K. Kim. Spider-web-inspired stretchable graphene woven fabric for highly sensitive, transparent, wearable strain sensors. *ACS Appl. Mater. Interfaces* **2019**, *11*, 2282-2294.

[21] J.H. Lee.; J.M. Kim.; D. Liu.; F.M. Guo.; X. Shen.; Q.B. Zheng.; S. Jeon.; J.K. Kim. Highly aligned, anisotropic carbon nanofiber films for multidirectional strain sensors with exceptional selectivity. *Adv. Funct. Mater.* **2019**, *29*, 1901623.

[22] H. Montazerian.; A. Rashidi.; A. Dalili.; H. Najjaran.; A. S. Milani.; M. Hoorfar. Graphene-coated spandex sensors embedded into silicone sheath for composites health monitoring and wearable applications. *Small* **2019**, *0*, 1804991.

[23] H. Song.; J. Zhang.; D. Chen.; K. Wang.; S. Niu.; Z. Han.; L. Ren. Superfast and high-sensitivity printable strain sensors with bioinspired micron-scale cracks. *Nanoscale* **2017**, *9*, 1166-1173.

[24] Q. D. Zhu.; K. V. Vliet.; N. H. Andersen.; A. Miserez. A double-layer mechanochromic hydrogel with multidirectional force sensing and encryption capability. *Adv. Funct. Mater.* **2019**, *29*, 1808191.

[25] M. Zhang.; C. Wang.; H. Wang.; M. Jian.; X. Hao.; Y. Zhang. Carbonized cotton fabric for high-performance wearable strain sensors. *Adv. Funct. Mater.* **2016**, *27*, 1604795.

[26] X. M. Li.; T. T. Yang.; Y. Yang.; J. Zhu.; L. Li.; F. E. Alam.; X. Li.; K. L. Wang.; H. Y. Cheng.; C. T. Lin.; Y. Fang.; H. W. Zhu. Large-area ultrathin graphene films by single-step marangoni self-assembly for highly sensitive strain sensing application. *Adv. Funct. Mater.* **2016**, *26*, 1322-1329.

[27] T. T. Yang.; W. Wang.; H. Z. Zhang.; X. M. Li.; J. D. Shi.; Y. J. He.; Q. S. Zheng.; Z. H. Li.; H. W. Zhu. Tactile sensing system based on arrays of graphene woven microfabrics: electromechanical behavior and electronic skin application. *ACS Nano* **2015**, *9*, 10867-10875.

[28] Y. Cheng.; R. R. Wang.; J. Sun.; L. Gao. A stretchable and highly sensitive graphene-based fiber for sensing tensile strain, bending, and torsion. *Adv. Mater.* **2015**, *27*, 7365-7371.

[29] Y. R. Jeong.; H. Park.; S. W. Jin.; S. Y. Hong.; S. S. Lee.; J. S. Ha. Highly stretchable and sensitive strain sensors using fragmentized graphene foam. *Adv. Funct. Mater.* **2015**, *25*, 4228-4236.

[30] Q. Liu.; J. Chen.; Y. R. Li.; G. Q. Shi. High-performance strain sensors with fish-scale-like graphene-sensing layers for full-range detection of human motions. *ACS Nano* **2016**, *10*, 7901-7906.

[31] H. Zhang.; D. Liu.; J. H. Lee.; H. Chen.; E. Y. Kim.; X. Shen.; Q. Zheng.; J. L. Yang.; J. K. Kim. Anisotropic, wrinkled, and crack-bridging structure for ultrasensitive, highly selective multidirectional strain sensors. *Nano-Micro Lett*. **2021**, *13*, 122.

[32] G. M. Yang.; X. Feng.; W. Wang.; Q. O. Yang.; L. Liu.; Z. J. Wu. Graphene and carbon nanotube-based high-sensitive film sensors for in-situ monitoring out-of-plane shear damage of epoxy composites. *Composites Part B: Engineering* **2021**, *204*, 108494.

[33] D. J. Lipomi.; M. Vosgueritchian.; B. C. K. Tee.; S. L. Hellstrom.; J. A. Lee.; C. H. Fox.; Z. N. Bao. Skin-like pressure and strain sensors based on transparent elastic films of carbon nanotubes. *Nat. Nanotechnol.* **2011**, *6*, 788-792.

[34] S. Tadakaluru.; W. Thongsuwan.; P. Singjai. Stretchable and flexible high-strain sensors made using carbon nanotubes and graphite films on natural rubber. *Sensors-Basel* **2014**, *14*, 868-876.

[35] E. Roh.; B. U. Hwang.; D. Kim.; B. Y. Kim.; N. E. Lee. Stretchable, Transparent, Ultrasensitive, and Patchable Strain Sensor for Human–Machine Interfaces Comprising a Nanohybrid of Carbon Nanotubes and Conductive Elastomers. *ACS Nano* **2015**, *9*, 6252-6261.

[36] H. Jang.; Y. J. Park.; X. Chen.; T. Das.; M. S. Kim.; J. H. Ahn. Graphene-based flexible and stretchable electronics. *Adv. Mater.* **2016**, *28*, 4184-4202.

[37] V. M. Pereira.; A. H. Castro Neto. Strain engineering of graphene's electronic structure. *Phys. Rev. Lett.* **2009**, *103*.

[38] M. Y. Huang.; T. A. Pascal.; H. Kim.; W. A. Goddard.; J. R. Greer. Electronic− mechanical coupling in graphene from in situ nanoindentation experiments and multiscale atomistic simulations. *Nano Lett.* **2011**, *11*, 1241-1246.

[39] J. F. Zang.; S. Ryu.; N. Pugno.; Q. M. Wang.; Q. Tu.; M. J. Buehler.; X. H. Zhao. Multifunctionality and control of the crumpling and unfolding of large-area graphene. *Nat. Mater.* **2013**, *12*, 321-325.

[40] S. H. Bae.; Y. Lee.; B. K. Sharma.; H. J. Lee.; J. H. Kim.; J. H. Ahn. Graphene-based transparent strain sensor. *Carbon* **2013**, *51*, 236-242.

[41] Y. Lee.; S. Bae.; H. Jang.; S. Jang.; S. E. Zhu.; S. H. Sim.; Y. I. Song.; B. H. Hong.; J. H. Ahn. Wafer-scale synthesis and transfer of graphene films. *Nano Lett.* **2010**, *10*, 490-493.

[42] J. Zhao.; C. L. He.; R. Yang.; Z. W. Shi.; M. Cheng.; W. Yang.; G. B. Xie.; D. M. Wang.; D. X. Shi.; G. Y. Zhang. Ultra-sensitive strain sensors based on piezoresistive nanographene films. *Appl. Phys. Lett.* **2012**, *101*.

[43] J. Zhao.; G. L. Wang.; R. Yang.; X. B. Lu.; M. Cheng.; C. L. He.; G. B. Xie.; J. L. Meng.; D. X. Shi.; G. Y. Zhang. Tunable piezoresistivity of nanographene films for strain sensing. *ACS Nano* **2015**, *9*, 1622-1629.

[44] J. Kuang.; L. Q. Liu.; Y. Gao.; D. Zhou.; Z. Chen.; B. H. Han.; Z. Zhang. A hierarchically structured graphene foam and its potential as a large-scale strain-gauge sensor. *Nanoscale* **2013**, *5*, 12171-12177.

[45] J. H. Li.; S. F. Zhao.; X. L. Zeng.; W. P. Huang.; Z. Y. Gong.; G. P. Zhang.; R. Sun.; C. P. Wong. Highly stretchable and sensitive strain sensor based on facilely prepared three-dimensional graphene foam composite. *ACS Appl. Mater. Inter.* **2016**, *8*, 18954-18961.

[46] X. Y. Cao.; J. Zhang.; S. W. Chen.; R. J. Varley.; K. Pan. 1D/2D nanomaterials synergistic, compressible, and response rapidly 3D graphene aerogel for piezoresistive sensor. *Adv. Funct. Mater.* **2020**, *30*, 2003618.

[47] M. Liao.; P. Wan.; J. Wen.; M. Gong.; X. Wu.; Y. Wang.; R. Shi.; L. Zhang. Wearable, healable, and adhesive epidermal sensors assembled from mussel-inspired conductive hybrid hydrogel framework. *Adv. Funct. Mater.* **2017**, *27*, 1703852.

[48] C. S. Boland.; U. Khan.; C. Backes.; A. O'Neill.; J. McCauley.; S. Duane.; R. Shanker.; Y. Liu.; I. Jurewicz.; A. B. Dalton.; J. N. Coleman. Sensitive, high-strain, high-rate bodily motion sensors based on graphene–rubber composites. *ACS Nano* **2014**, *8*, 8819-8830.

[49] J. R. Huang.; X. X. Yang.; S. C. Her.; Y. M. Liang. Carbon nanotube/graphene nanoplatelet hybrid film as a flexible multifunctional sensor. *Sensors (Basel).* **2019**, *19*, 317.

[50] Q. B. Zheng.; M. M. Gudarzi.; S. J. Wang.; Y. Geng.; Z. G. Li.; J. K. Kim. Improved electrical and optical characteristics of transparent graphene thin films produced by acid and doping treatments. *Carbon* **2011**, *49*, 2905-2916.

[51] X. Y. Lin.; X. Shen.; Q. B. Zheng.; N. Yousefi.; L. Ye.; Y. W. Mai.; J. K. Kim. Fabrication of highly-aligned, conductive, and strong graphene papers using ultralarge graphene oxide sheets. *ACS Nano* **2012**, *6*, 10708-10719.

[52] Q. B. Zheng.; Z. G. Li.; J. H. Yang.; J. K. Kim. Graphene oxide-based transparent conductive films. *Prog. Mater. Sci.* **2014**, *64*, 200-247.

[53] S. K. Deng.; V. Berry. Wrinkled, rippled and crumpled graphene: an overview of formation mechanism, electronic properties, and applications. *Mater. Today* **2016**, *19*, 197-212.

[54] S. H. Aboutalebi.; M. M. Gudarzi.; Q. B. Zheng.; J. K. Kim. Spontaneous formation of liquid crystals in ultralarge graphene oxide dispersions. *Adv. Funct. Mater* **2011**, *21*, 2978-2988.

[55] J. Huang.; J. Zhou.; Y. M. Luo.; G. Yan.; Y. Liu.; Y. P. Shen.; Y. Xu.; H. L. Li.; L. B. Yan.; G. H. Zhang.; Y. Q. Fu.; H. G. Duan. Wrinkle-enabled highly stretchable strain sensors for wide-

range health monitoring with a big data cloud platform. *ACS Appl. Mater. Interfaces* **2020**, *12*, 43009−43017.

[56] H. L. Sun.; K. Dai.; W. Zhai.; Y. J. Zhou.; J. W. Li.; J. Q. Zheng.; B. Li.; C. T. Liu.; C. Y. Shen. A highly sensitive and stretchable yarn strain sensor for human motion tracking utilizing a wrinkle-assisted crack structure. *ACS Appl. Mater. Interfaces* **2019**, *11*, 36052−36062.

[57] S. Choi.; S. Lee.; B. Lee.; T. Kim.; Y. Hong. Selective crack formation on stretchable silver nano-particle based thin films for customized and integrated strain-sensing system. *Thin Solid Films* **2020**, *707*, 138068.

[58] Z. M. Chu.; W. C. Jiao.; Y. F. Huang.; Y. T. Zheng.; R. J. Wang.; X. D. He. Superhydrophobic gradient wrinkle strain sensor with ultra-high sensitivity and broad strain range for motion monitoring. *J. Mater. Chem. A* **2021**, *9*, 9634.

[59] K. H. Kim.; S. K. Hong.; S. H. Ha.; L. H. Li.; H. W. Lee.; J. M. Kim. Enhancement of linearity range of stretchable ultrasensitive metal crack strain sensor via superaligned carbon nanotube-based strain engineering. *Mater. Horiz.* **2020**,*7*, 2662.

[60] N. Zhao.; Z. Wang.; C. Cai.; H. Shen.; F. Y. Liang.; D. Wang.; C. Y. Wang.; T. Zhu.; J. Guo.; Y. X. Wang.; X. F. Liu.; C. T. Duan.; H. Wang.; Y. Z. Mao.; X. Jia.; H. X. Dong.; X. L. Zhang.; J. Xu. Bioinspired materials: from low to high dimensional structure. *Adv. Mater.* **2014**, *26*, 6994-7017.

[61] Q. Zou.; J. Zheng.; Q. Su.; W. L. Wang.; W. Gao.; Z. M. Ma. A wave-inspired ultrastretchable strain sensor with predictable cracks. *Sens. Actuator A Phys.* **2019**, 300, 111658